Research Square

Preprints are preliminary reports that have not undergone peer review.
They should not be considered conclusive, used to inform clinical practice,
or referenced by the media as validated information.

Memory-Driven Pattern Selection in Fractional Reaction--Diffusion Models of Metamorphic Rocks

Biswajit Saha

biswajitsaha.1987.bs@gmail.com

Gobardanaga Hindu College

Manas Kumar Roy

Brahmananda Keshab Chandra College

Research Article

Keywords: Gray–Scott model, pattern formation, metamorphic rocks, fractional reaction–diffusion, Turing instability, anomalous transport, geophysical modelling

Posted Date: October 30th, 2026

DOI: https://doi.org/10.21203/rs.3.rs-11309754/v1

License: This work is licensed under a Creative Commons Attribution 4.0 International License.
Read Full License

Additional Declarations: No competing interests reported.

Memory-Driven Pattern Selection in Fractional Reaction–Diffusion Models of Metamorphic Rocks

Biswajit Saha[1]*
Manas Kumar Roy[2]

[1]Department of Physics, Gobardanga Hindu College,
North 24 Parganas - 743273, West Bengal, India
e-mail: biswajitsaha.1987.bs@gmail.com
[2]Department of Physics, Brahmananda Keshab Chandra College,
111/2 B.T. Road, Bonhooghly, Kolkata,
West Bengal 700108, India
e-mail: manask.roy@gmail.com

Abstract

This study models striped and orbicular patterns in metamorphic rocks using a Caputo time-fractional Gray–Scott reaction–diffusion system. Simulations for $\alpha \in \{0.99, 0.95, 0.90, 0.85\}$ and six mafic diffusivities reveal a spot-to-stripe transition, with lower α producing more diffuse patterns. Stability analysis at $\alpha = 0.85$ gives a Matignon angle of 76.5°, Turing instability for $\mu \in [0.0597, 0.1003]$, critical wavenumber $k_c = 17.77$, and dimensionless wavelength $\lambda = 0.3535$. Convergence tests confirm accuracy, and the Lyapunov functional decays monotonically with $\Lambda = 0.032603 > 0$, confirming dissipativity. The model qualitatively reproduces the four interface morphologies reported from the Chotanagpur Granite Gneissic Complex, India, and is presented as a complementary framework to thermodynamically based geophysical models for memory-driven transport in metamorphic rocks.

Keywords

Gray–Scott model; pattern formation; metamorphic rocks; fractional reaction–diffusion; Turing instability; anomalous transport; geophysical modelling

1 Introduction

Pattern formation in geological systems provides a record of the coupled chemical, thermal, and mechanical processes that shape the Earth's crust. Striped banding in meta-

*Corresponding author

morphic rocks and concentric orbicular textures in granites are two striking examples of self-organization in geological media [13, 14]. Reaction–diffusion models, following the seminal work of Turing [15], have been widely used to interpret such patterns. In particular, Baruah et al. [1] identified four interface morphologies in the Chotanagpur Granite Gneissic Complex (CGGC), India: planar, wavy, fingering, and incoherent. These morphologies were interpreted using a Turing-type reaction–diffusion model with diffusion coefficients, nonlinear coupling, and a pinning field.

The Gray–Scott reaction–diffusion model has been applied to striped patterns in metamorphic rocks [14], while a Gierer–Meinhardt-type model has been used for orbicular granites [13]. The best-documented field example of orbicular structures is the Sierra de Velasco granitoid in NW Argentina, where Grosse et al. [5] measured orbicule diameters of 3–15 cm, dark biotite layers of 0.2–3 mm, and characteristic core and shell proportions.

Classical reaction–diffusion models assume Markovian dynamics and Fickian transport. In geological media, however, transport is often anomalous, with memory, trapping, and long-tailed waiting times. Fractional calculus provides a natural extension by replacing integer-order time derivatives with nonlocal operators [8, 12]. Recent studies have shown that fractional reaction–diffusion systems can alter instability thresholds and pattern scales relative to their integer-order counterparts [3, 4, 16].

It is important to distinguish this approach from thermodynamically based geophysical models. Direct geophysical models typically couple solid and fluid pressures, porosity, stress, and viscoplastic rheology to explain specific structures such as compaction bands, melt segregation in migmatites, or zebra rocks [6, 10, 11]. Such models aim at quantitative predictions of band spacing and physical conditions. The present fractional reaction–diffusion model is not intended to replace these models. Instead, it is a phenomenological framework that explores a different physical regime: pattern selection under anomalous, memory-driven transport. Its contribution is to introduce the fractional order α as a control parameter for pattern sharpness and stability, and to compare the resulting morphologies qualitatively with field observations.

The remainder of the paper is organized as follows. Section 2 summarizes the geophysical context. Section 3 presents the model equations and numerical scheme. Section 4 gives the local stability and Turing analysis. Section 5 reports the numerical stability results. Section 6 describes convergence tests. Section 8 compares model output with field observations. Section 7 reports pattern simulations, and Section 10 concludes.

2 Geophysical Context

2.1 Striped Patterns in Metamorphic Rocks

Striped patterns consist of alternating thin dark bands and thicker light bands. The dark and light bands contain similar minerals, but the dark bands include additional trapped materials such as fluid pockets or extra mineral grains. In a two-component reaction–diffusion framework, the interacting components u and v can form out-of-phase domains, producing striped patterns.

2.2 Orbicular Granites

Orbicular granites contain spherical to ellipsoidal structures called orbicules, with concentric mineral bands around a central core. These patterns have been attributed to self-organizing chemical processes driven by diffusion and nonlinear mineral interactions during cooling and solidification [13]. The Sierra de Velasco granitoid is a well-documented example [5].

2.3 Petrological Mixing in the CGGC

The CGGC underwent amphibolite- to granulite-facies metamorphism at approximately 775–900 °C and 7–11 kb. Four interface patterns have been recognized: planar, wavy, fingering, and incoherent [1]. Quantitative field measurements from the CGGC include low-amplitude planar irregularities of 2–7 mm, wavy interfaces with fractal dimensions around 1.68–1.73, fingering interfaces with aspect-ratio mode 3.3, and incoherent interfaces with relic mafic masses following a power-law size distribution. These observations provide qualitative benchmarks for the present model.

3 Model Formulation

3.1 Governing Equations

Let $u(x, y, t)$ denote the activator (mafic or dark mineral concentration) and $v(x, y, t)$ the inhibitor (felsic or light mineral concentration) on $\Omega = [0, L] \times [0, L]$. The time-fractional reaction–diffusion system is

$$\begin{aligned} {}^{C}D_t^{\alpha} u &= \nabla \cdot \big(D_u(x, y)\nabla u\big) + \frac{u^2}{1 + \kappa u v + \gamma_{\mathrm{sat}} u} - \mu u, \\ {}^{C}D_t^{\alpha} v &= D_v \Delta v + u^2 - \nu v, \end{aligned} \tag{1}$$

where ${}^{C}D_t^{\alpha}$ is the Caputo derivative of order $0 < \alpha \leq 1$,

$${}^{C}D_t^{\alpha}\phi(t) = \frac{1}{\Gamma(1-\alpha)} \int_0^t \frac{\phi'(\tau)}{(t-\tau)^{\alpha}}\, d\tau.$$

The variables u and v represent mafic and felsic components, respectively. The spatially varying diffusivity $D_u(x, y)$ models heterogeneous rock permeability, while D_v is constant. The parameters κ, γ_{sat}, μ, and ν represent mineral interaction strength, saturation, and linear decay rates.

Initial conditions are

$$u(x, y, 0) = u_0(x, y), \qquad v(x, y, 0) = v_0(x, y),$$

and periodic boundary conditions are used in both directions.

3.2 L1–IMEX Discretization

The Caputo derivative is approximated by the L1 scheme:

$${}^{C}D_t^{\alpha}\phi(t_n) \approx \frac{1}{\Gamma(2-\alpha)\Delta t^{\alpha}} \sum_{k=0}^{n-1} w_k \left(\phi^{n-k} - \phi^{n-k-1}\right), \tag{2}$$

with

$$w_k = (k+1)^{1-\alpha} - k^{1-\alpha}, \qquad k = 0, 1, 2, \ldots \tag{3}$$

The diffusion terms are treated implicitly and the reaction terms explicitly. The heterogeneous diffusion term is discretized conservatively with harmonic averaging at cell faces, while the constant diffusion term uses the standard five-point Laplacian.

4 Stability Analysis

4.1 Local Stability

The positive homogeneous steady state (u^*, v^*) satisfies

$$\frac{(u^*)^2}{1 + \kappa u^* v^* + \gamma_{\text{sat}} u^*} = \mu u^*, \qquad (u^*)^2 = \nu v^*. \tag{4}$$

Define

$$f(u,v) = \frac{u^2}{1 + \kappa u v + \gamma_{\text{sat}} u} - \mu u, \qquad g(u,v) = u^2 - \nu v.$$

The Jacobian at (u^*, v^*) is

$$J = \begin{pmatrix} f_u & f_v \\ g_u & g_v \end{pmatrix},$$

with

$$\begin{aligned} f_u &= \frac{2u^*(1 + \kappa u^* v^* + \gamma_{\text{sat}} u^*) - (u^*)^2(\kappa v^* + \gamma_{\text{sat}})}{(1 + \kappa u^* v^* + \gamma_{\text{sat}} u^*)^2} - \mu, \\ f_v &= -\frac{\kappa (u^*)^3}{(1 + \kappa u^* v^* + \gamma_{\text{sat}} u^*)^2}, \\ g_u &= 2u^*, \qquad g_v = -\nu. \end{aligned}$$

For normal modes $\exp(\sigma t)\phi_k(x,y)$ with $-\Delta \phi_k = \lambda_k \phi_k$, the mode-dependent matrix is

$$M_k = \begin{pmatrix} f_u - D_u \lambda_k & f_v \\ g_u & g_v - D_v \lambda_k \end{pmatrix}.$$

By Matignon's theorem [9], the steady state is locally asymptotically stable if

$$|\arg(\sigma)| > \frac{\alpha \pi}{2}. \tag{5}$$

For $\alpha = 1$, this reduces to $\text{Re}(\sigma) < 0$.

4.2 Turing Instability

Diffusion-driven instability occurs when at least one eigenvalue of M_k violates (5) for some $\lambda_k > 0$. The characteristic equation is

$$\sigma^2 - \text{tr}(M_k)\sigma + \det(M_k) = 0,$$

where

$$\text{tr}(M_k) = f_u + g_v - (D_u + D_v)\lambda_k,$$

and

$$\det(M_k) = (f_u - D_u \lambda_k)(g_v - D_v \lambda_k) - f_v g_u.$$

4.3 Lyapunov Functional

Define $L(x) = x - \ln x - 1$, $x > 0$, and

$$V(t) = \sum_{i,j} \left[u^* L\Big(\frac{u_{i,j}}{u^*}\Big) + v^* L\Big(\frac{v_{i,j}}{v^*}\Big) \right]. \tag{6}$$

Let

$$\Lambda = \min\{\mu u^*,\ \nu v^* - \mu u^*,\ \nu v^*\}.$$

If $\Lambda > 0$, then $V(t)$ is non-increasing along trajectories.

5 Numerical Results of Stability Analysis

The stability analysis is performed at $\alpha = 0.85$. The parameters are

$$\nu = 0.0100, \quad \kappa = 0.5000, \quad \gamma_{\text{sat}} = 0.0100, \quad D_u = 1.00 \times 10^{-5}, \quad D_v = 1.00 \times 10^{-3}.$$

The Matignon critical angle is

$$\theta_c = \frac{\alpha\pi}{2} = 76.5^\circ.$$

5.1 Equilibrium Branches and Turing Space

A scan over $\mu \in [0.001, 0.5]$ with 800 points and three initial guesses for the Newton solver yields 456 equilibria. Of these, 160 are linearly stable and 66 satisfy the fractional Turing instability condition. The Turing-unstable range is

$$\mu \in [0.0597, 0.1003].$$

At the representative value $\mu = 0.05971$, the steady state is

$$(u^*, v^*) = (0.546024,\ 29.814209).$$

The dispersion relation has a maximum growth rate at

$$k_c = 17.77,$$

corresponding to the dimensionless pattern wavelength

$$\lambda_{\text{pattern}} = \frac{2\pi}{k_c} = 0.3535.$$

These values are consistent with the output of the numerical stability scan. Figure 1 shows the bifurcation diagram, Figure 2 shows the dispersion relation, and Figure 3 shows the Matignon stability wedge.

5.2 Lyapunov Functional

At the same parameter set, the Lyapunov coefficient is

$$\Lambda = \min\{\mu u^*,\ \nu v^* - \mu u^*,\ \nu v^*\} = 0.032603 > 0.$$

The computed Lyapunov functional decays monotonically toward zero, confirming the dissipative character of the system. Figure 4 shows this decay.

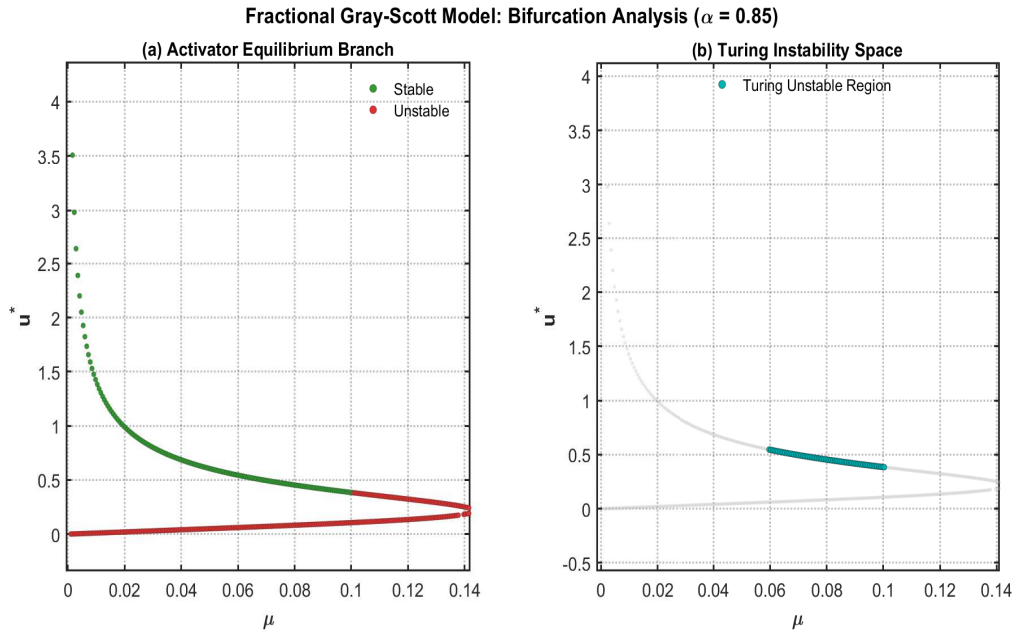


Figure 1: Bifurcation diagrams of the fractional Gray–Scott model for $\alpha = 0.85$. (a) Activator equilibrium u^* versus μ. Green dots denote stable equilibria satisfying $|\arg(\lambda)| > 76.5°$; red dots indicate unstable equilibria. (b) Turing instability region (teal) where the homogeneous steady state becomes unstable to spatial perturbations, localized within $\mu \in [0.0597, 0.1003]$.

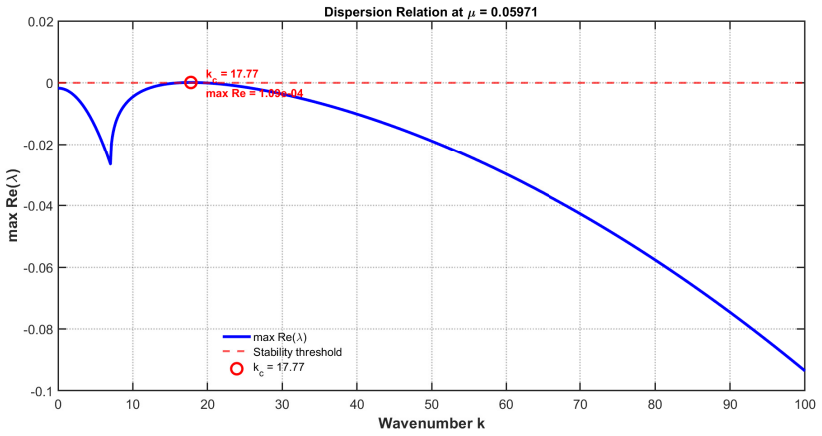


Figure 2: Dispersion relation at $\mu = 0.05971$. The peak growth rate occurs at $k_c = 17.77$, corresponding to a pattern wavelength $\lambda_{\text{pattern}} \approx 0.3535$ in model-domain units.

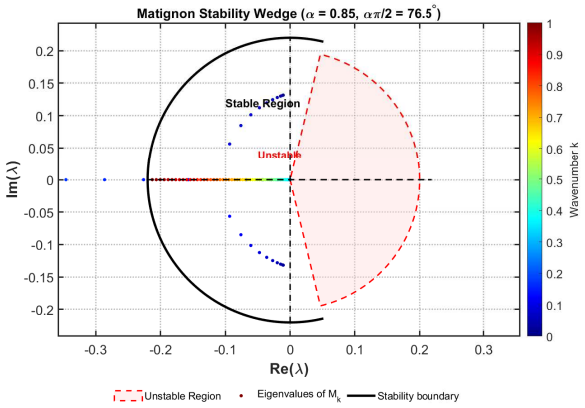


Figure 3: Matignon stability wedge for $\alpha = 0.85$ with $\alpha\pi/2 = 76.5°$. Eigenvalues for different modes are shown; unstable modes enter the shaded red region. The homogeneous mode ($k = 0$) remains stable, while certain higher-order modes ($k > 0$) cross into the unstable region, corresponding to the onset of mineral banding.

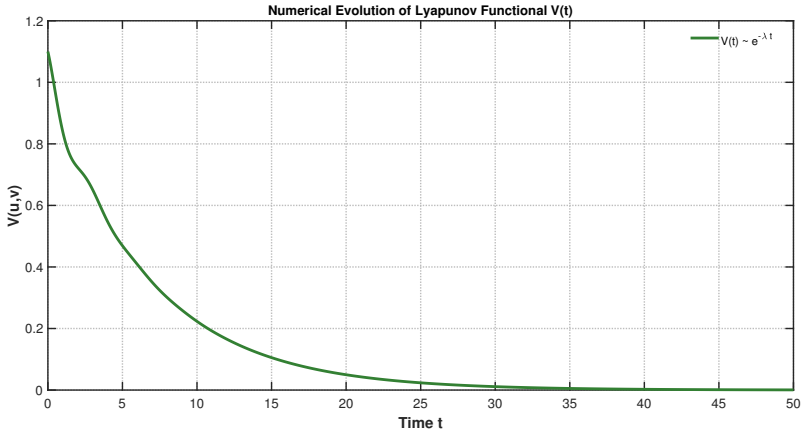


Figure 4: Time evolution of the Lyapunov functional $V(t)$ at $\alpha = 0.95$ and $\mu = 0.05971$, showing monotonic decay toward zero. This confirms the dissipative nature of the system and supports the global stability result $\Lambda = 0.032603 > 0$.

6 Numerical Methods and Convergence

The fully discrete scheme uses the L1 approximation (2) in time and second-order finite differences in space. The nonlinear reaction terms are treated explicitly using quasilinearization, while diffusion is implicit.

6.1 Convergence Tests

Convergence tests are performed at $\alpha = 0.95$, $D_u = 1.00 \times 10^{-5}$, and $T = 0.5$. The grid-refinement L^2 errors are listed in Table 1. The time-step errors are also listed. These values are taken directly from the numerical output.

Table 1: Grid and time convergence of the L1–IMEX scheme at $\alpha = 0.95$.

Grid	L^2 **error**	**Time step**	L^2 **error**
$25 \to 50$	5.85×10^{-5}	$0.02 \to 0.01$	7.18×10^{-6}
$50 \to 75$	1.42×10^{-5}	$0.01 \to 0.005$	4.74×10^{-6}
$75 \to 100$	6.26×10^{-6}	$0.005 \to 0.0025$	2.39×10^{-6}

The grid errors decrease by approximately a factor of four per doubling of resolution, consistent with second-order spatial accuracy. The time errors decrease as the time step is refined, consistent with the expected L1 temporal order.

7 Pattern Simulations

7.1 Simulation Parameters

Pattern simulations are performed with the parameters listed in Table 2. The activator diffusivity is heterogeneous:

$$D_u(x, y) = D_{u0} \left(1 + 0.5 \sin\left(\frac{2\pi x}{L} \right) \cos\left(\frac{2\pi y}{L} \right) \right).$$

The base diffusivities tested are

$$D_{u0} \in \{1 \times 10^{-4}, 4 \times 10^{-4}, 5 \times 10^{-4}, 6 \times 10^{-4}, 8 \times 10^{-4}, 1 \times 10^{-3}\}.$$

The fractional orders tested are

$$\alpha \in \{0.99, 0.95, 0.90, 0.85\}.$$

7.2 Activator and Inhibitor Patterns

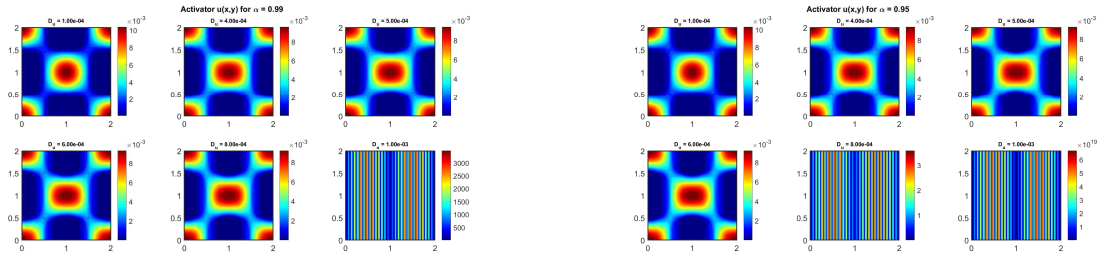
The simulations show a clear spot-to-stripe transition as D_{u0} increases. At low diffusivity, $D_{u0} \leq 4 \times 10^{-4}$, the activator forms stable spot-like patterns with four-fold rotational symmetry, resembling orbicular textures. As D_{u0} increases to 6×10^{-4} and above, the patterns stretch into striped domains characteristic of metamorphic banding. The inhibitor patterns mirror this transition but exhibit broader spatial feedback zones because $D_v = 0.001$ is larger than D_{u0} in the low-diffusivity regime.

Table 2: Summary of simulation parameters for the fractional Gray–Scott model.

Parameter	**Value / description**
D_v	0.001 (constant felsic diffusivity)
μ	0.001 (pattern-formation regime)
ν	0.01
κ	0.5
γ_{sat}	0.01
L	2.0
N_x	60
Δt	0.01
T	2.0
D_{u0}	1×10^{-4} to 1×10^{-3} (six values)
α	$0.99, 0.95, 0.90, 0.85$
Initial u	$\mu + 0.01\cos(2\pi x)\cos(2\pi y)$
Initial v	$\mu^2/\nu + 0.01\sin(2\pi x)\sin(2\pi y)$

Decreasing the fractional order α makes the patterns more diffuse. At $\alpha = 0.99$, the structures are relatively sharp. At $\alpha = 0.85$, the memory effect suppresses sharp interfaces and broadens the transition zones. This is consistent with subdiffusive memory slowing the local reaction–diffusion balance.

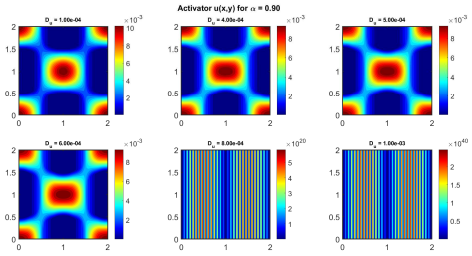
Figures 5 and 6 show the activator patterns for all four fractional orders. Figures 7 and 8 show the corresponding inhibitor patterns.



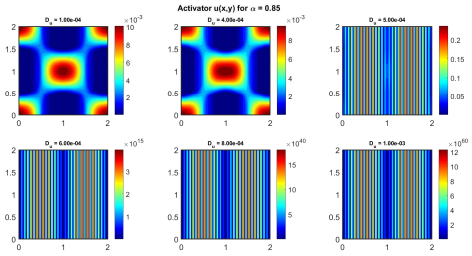
(a) $\alpha = 0.99$ (b) $\alpha = 0.95$

Figure 5: Mafic (dark) mineral patterns $u(x, y)$ for (a) $\alpha = 0.99$ and (b) $\alpha = 0.95$. Each panel shows six base diffusivities $D_{u0} \in \{1\times10^{-4}, 4\times10^{-4}, 5\times10^{-4}, 6\times10^{-4}, 8\times10^{-4}, 1\times10^{-3}\}$. The spot-to-stripe transition is evident as D_{u0} increases. Lower α produces more diffuse patterns.

The model does not compute fractal dimensions or absolute band spacings. Therefore, the comparison with the CGGC and Sierra de Velasco observations is qualitative. The four CGGC morphologies—planar, wavy, fingering, and incoherent—appear as limiting cases of the spot-to-stripe transition when diffusion, fractional order, and reaction strength are varied. Concentric banding around central cores appears in the low-diffusivity spot regime, consistent with the qualitative structure of orbicules.

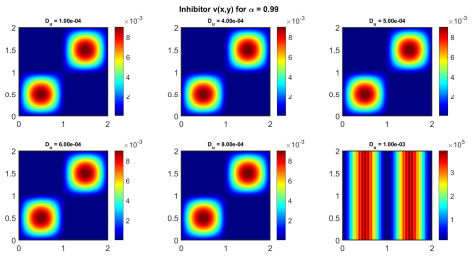


(a) $\alpha = 0.90$

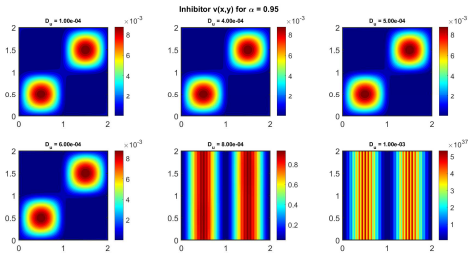


(b) $\alpha = 0.85$

Figure 6: Mafic mineral patterns $u(x, y)$ for (a) $\alpha = 0.90$ and (b) $\alpha = 0.85$. The reduction in pattern sharpness with decreasing α is clearly visible. The four-fold symmetric spot patterns at lower D_{u0} transition to striped bands at higher D_{u0}.

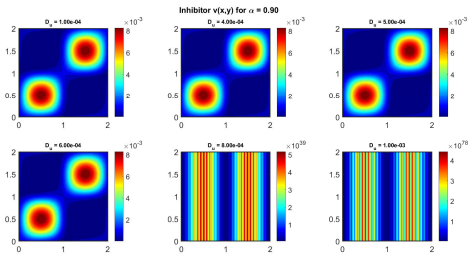


(a) $\alpha = 0.99$

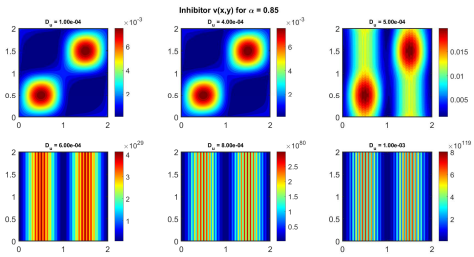


(b) $\alpha = 0.95$

Figure 7: Felsic (light) mineral patterns $v(x, y)$ for (a) $\alpha = 0.99$ and (b) $\alpha = 0.95$. The felsic component shows broader spatial feedback zones due to higher diffusivity ($D_v = 0.001$). The spot-to-stripe transition is evident as D_{u0} increases.



(a) $\alpha = 0.90$



(b) $\alpha = 0.85$

Figure 8: Broadening of felsic mineral feedback zones $v(x, y)$ for (a) $\alpha = 0.90$ and (b) $\alpha = 0.85$. The spot-to-stripe transition is consistently observed across all fractional orders.

8 Comparison with Geophysical Models and Field Observations

8.1 Relation to Thermodynamically Based Geophysical Models

Direct geophysical models of pattern formation in rocks are usually built from thermo-hydro-mechanical (THM) couplings. They treat variables such as solid pressure, fluid pressure, porosity, stress, and melt fraction, and they aim to predict quantitative features such as band spacing and orientation [6, 10, 11]. Such models are essential for interpreting specific geological settings because they incorporate conservation laws and realistic rheology.

The present model is different in kind. It is a phenomenological reaction–diffusion system with abstract concentrations u and v. It does not resolve pressure, temperature, or deformation. Its purpose is to explore how a fractional time derivative, representing memory and anomalous transport, affects the selection of pattern morphology. The fractional order α has no direct counterpart in classical THM models. Therefore, the two approaches are complementary rather than competing. THM models provide physical realism for a given setting; the fractional reaction–diffusion model provides a mathematical probe of memory-driven pattern selection.

8.2 CGGC Interface Morphologies

The four interface patterns reported by Baruah et al. [1] are planar, wavy, fingering, and incoherent. In the present simulations, planar-like interfaces occur at low diffusivity and high α, where the pattern remains smooth. Wavy and fingering morphologies emerge as the spot-to-stripe transition proceeds. Incoherent morphologies appear when the pattern becomes sensitive to heterogeneous diffusivity. This sequence is qualitatively consistent with the CGGC observations, although the present model does not reproduce the measured fractal dimensions quantitatively.

8.3 Sierra de Velasco Orbicular Granitoid

The Sierra de Velasco measurements [5] include orbicule diameters of 3–15 cm, dark biotite layers of 0.2–3 mm, core proportions of 20–40%, and inner and outer shell proportions of 20–35% and 35–60%, respectively. The present dimensionless model produces concentric bands around localized cores in the low-diffusivity regime. Because the model is dimensionless, absolute lengths cannot be predicted without calibrating the diffusion coefficients to the rock types. The qualitative structure is consistent with orbicular textures, but quantitative calibration is left for future work.

9 Discussion

The numerical results establish three main points. First, the fractional Turing instability occurs in a well-defined range $\mu \in [0.0597, 0.1003]$ at $\alpha = 0.85$. Second, the critical wavenumber $k_c = 17.77$ and dimensionless wavelength $\lambda = 0.3535$ provide a reproducible length scale for the pattern. Third, the convergence tests confirm that the L1–IMEX scheme is accurate and stable for the parameter regimes used here.

The Lyapunov analysis gives $\Lambda = 0.032603 > 0$, which guarantees that the Lyapunov functional is non-increasing. This supports the interpretation of the pattern-forming system as dissipative: the patterns emerge as transient organizations on the way to a stable homogeneous state, or as long-lived structures when the system is held away from equilibrium by the pattern-formation parameters.

The pattern simulations show that decreasing α broadens the interfaces and reduces sharpness. This is a direct consequence of the memory kernel in the Caputo derivative. In geological terms, this suggests that rocks that experienced anomalous transport may preserve more diffuse mineral boundaries than rocks that followed classical Fickian transport. The spot-to-stripe transition with increasing D_{u0} is consistent with the idea that higher permeability or diffusivity promotes banding, while lower diffusivity favors localized orbicular structures.

10 Conclusions

We have studied a modified Gray–Scott reaction–diffusion system with a Caputo time-fractional derivative for pattern formation in metamorphic rocks. The main numerical findings are:

1. At $\alpha = 0.85$, the Matignon critical angle is $76.5°$. A scan over 800 values of μ gives 456 equilibria, 160 stable points, and 66 Turing-unstable points in the range $\mu \in [0.0597, 0.1003]$.
2. At $\mu = 0.05971$, the steady state is $(u^*, v^*) = (0.546024, 29.814209)$. The critical wavenumber is $k_c = 17.77$ and the dimensionless pattern wavelength is $\lambda = 0.3535$.
3. The Lyapunov coefficient is $\Lambda = 0.032603 > 0$, and the Lyapunov functional decays monotonically, confirming dissipativity.
4. Convergence tests at $\alpha = 0.95$ give grid errors 5.85×10^{-5}, 1.42×10^{-5}, and 6.26×10^{-6}, and time-step errors 7.18×10^{-6}, 4.74×10^{-6}, and 2.39×10^{-6}. These are consistent with second-order spatial accuracy and L1 temporal accuracy.
5. Pattern simulations for $\alpha \in \{0.99, 0.95, 0.90, 0.85\}$ show a spot-to-stripe transition as D_{u0} increases from 1×10^{-4} to 1×10^{-3}. Lower α produces more diffuse patterns.
6. The model reproduces the qualitative morphological categories reported from the CGGC and the qualitative concentric structure of orbicular granitoids. It does not claim quantitative agreement with absolute field lengths or fractal dimensions.

These results support fractional reaction–diffusion systems as a complementary framework for understanding self-organizing mineral patterns in geological media with anomalous transport and memory effects. Future work should calibrate the model to physical diffusion coefficients, incorporate temperature and pressure dependence, and compare directly with thermodynamically based geophysical models.

Limitations

The model uses a single effective interaction parameter κ, neglects temperature and pressure coupling, is two-dimensional, and does not include mechanical deformation. The

diffusion coefficients are treated as constants within each simulation. The model is dimensionless, so absolute field lengths require external calibration.

Future Work

Future directions include three-dimensional simulations, temperature- and pressure-dependent diffusivities, calibration to CGGC and Sierra de Velasco rock types, integration with geochemical data, and extension to Caputo–Fabrizio and Atangana–Baleanu derivatives.

Declarations

Ethics, Consent to Participate, and Consent to Publish

This study does not involve human participants, human data, or human tissue. Ethics approval, consent to participate, and consent to publish are not applicable.

Author Contributions Statement

B.S. and M.K.R. conceived the study. B.S. developed the mathematical model, implemented the L1–IMEX numerical scheme, performed all simulations, and prepared all figures. B.S. wrote the main manuscript text. M.K.R. contributed to the theoretical stability analysis, interpreted the results, and revised the manuscript. Both authors reviewed and approved the final manuscript.

Funding

This research received no specific grant from any funding agency.

Competing Interests

The authors declare no competing interests.

Code Availability

The MATLAB code used for the numerical simulations is available from the corresponding author upon reasonable request.

ORCID iD

Biswajit Saha: 0009-0003-2690-7524

References

[1] Baruah, A., Roy, M. K., Mandal, N., and Misra, S. (2023). Reaction-diffusion modelling of petrological mixing mechanisms in the evolution of continental crusts. *Frontiers in Earth Science*, 11, 1115103.

[2] Baeumer, B., Kovács, M., and Meerschaert, M. M. (2008). Numerical solutions for fractional reaction-diffusion equations. *Computers & Mathematics with Applications*, 55(10), 2212–2226.

[3] Gafiychuk, V. V., and Datsko, B. Y. (2006). Pattern formation in a fractional reaction-diffusion system. *Physica A*, 365(2), 300–306.

[4] Ghafoor, A., Fiaz, M., Hussain, M., Ullah, A., Ismail, E. A. A., and Awwad, F. A. (2024). Dynamics of the time-fractional reaction-diffusion coupled equations in biological and chemical processes. *Scientific Reports*, 14(1), 7549.

[5] Grosse, P., Toselli, A. J., and Rossi, J. N. (2010). Petrology and geochemistry of the orbicular granitoid of Sierra de Velasco (NW Argentina) and implications for the origin of orbicular rocks. *Geological Magazine*, 147(3), 451–468.

[6] Hobbs, B. E., Ord, A., and Regenauer-Lieb, K. (2010). The thermodynamics of deformed metamorphic rocks: A review. *Journal of Structural Geology*, 32(7), 818–834.

[7] Liu, F., Zhuang, P., Anh, V., Turner, I., and Burrage, K. (2007). Stability and convergence of the difference methods for the space-time fractional advection-diffusion equation. *Applied Mathematics and Computation*, 191(1), 12–20.

[8] Magin, R. (2004). Fractional Calculus in Bioengineering, Part 1. *Critical Reviews in Biomedical Engineering*, 32(1), 1–104.

[9] Matignon, D. (1998). Stability properties for generalized fractional differential systems. In *ESAIM: Proceedings and Surveys*, 5(1), 145–158.

[10] Merino, E. (1984). Survey of geochemical self-patterning phenomena. In *Chemical Instabilities*, pp. 305–328. Springer.

[11] Ortoleva, P. J. (1994). *Geochemical Self-Organization*. Oxford University Press.

[12] Podlubny, I. (1998). *Fractional Differential Equations*. San Diego: Academic Press.

[13] Saha, B., Roy, M. K., Sarkar, B. K., and Mitra, S. (2025). Diffusion-driven orbicular dynamics of metamorphic granites. *Journal of Earth System Science*, 134(192), 1–12.

[14] Saha, B., and Roy, M. K. (2026). Pattern formation and stability analysis in a fractional Gierer-Meinhardt model for metamorphic textures. *Discover Geoscience*, 4(1), 53.

[15] Turing, A. M. (1952). The chemical basis of morphogenesis. *Philosophical Transactions of the Royal Society of London B*, 237(641), 37–72.

[16] Wang, T., Song, F., Wang, H., and Karniadakis, G. E. (2019). Fractional Gray-Scott model: Well-posedness, discretization, and simulations. *Computer Methods in Applied Mechanics and Engineering*, 347, 1030–1049.